

Floquet quantum state manipulation of a short Rydberg atom array

Jiahui Zhang(张佳慧), Liping Li(李利平), Yongjian Wang(王永建), Bo Wang(王博)

Citation: Chin. Phys. B.2026. 35(**8**): 083205. DOI: 10.1088/1674-1056/ae4c70
http://cpb.iphy.ac.cn; http://iopscience.iop.org/cpb

What follows is a list of articles you may be interested in

Robust excitation of ^{229}Th via generalized composite pulses: Compensating generic errors across arbitrary pulse shapes

Rui Zhao(赵睿) and Yingdan Wang(王颖丹)
Chin. Phys. B, 2026, 35 (**6**): 063201. DOI: 10.1088/1674-1056/ae4e8d

Measuring the Coulomb time shift in high-order harmonic generation

Shengjun Yue(岳生俊), Siqi Song(宋思琦), Ruofeng Zhong(钟若峰), Jiangkun Li(李江坤), Haiyuan Yu(于海元), and Hongchuan Du(杜洪川)
Chin. Phys. B, 2026, 35 (**4**): 043201. DOI: 10.1088/1674-1056/ae1951

Nondestructive detection of atom counts in laser-trapped ^{171}Yb atoms

Congcong Tian(田聪聪), Qiang Zhu(朱强), Bing Wang(王兵), Dezhi Xiong(熊德智), Zhuanxian Xiong(熊转贤), Lingxiang He(贺凌翔), and Baolong Lyu(吕宝龙)
Chin. Phys. B, 2025, 34 (**2**): 023201. DOI: 10.1088/1674-1056/ad9e9d

A miniaturized spin-exchange relaxation-free atomic magnetometer based on uniform light field

Jiajie Li(李佳洁), Xiujie Fang(房秀杰), Renjie Li(李任杰), Baodong Chen(陈宝栋), Yueyang Zhai(翟跃阳), and Ying Liu(刘颖)
Chin. Phys. B, 2023, 32 (**5**): 053201. DOI: 10.1088/1674-1056/aca7f2

Integrated, reliable laser system for an ^{87}Rb cold atom fountain clock

Zhen Zhang(张镇), Jing-Feng Xiang(项静峰), Bin Xu(徐斌), Pan Feng(冯盼), Guang-Wei Sun(孙广伟),Yi-Ming Meng(孟一鸣), Si-Min-Da Deng(邓思敏达), Wei Ren(任伟),Jin-Yin Wan(万金银), and De-Sheng Lü(吕德胜)
Chin. Phys. B, 2023, 32 (**1**): 013202. DOI: 10.1088/1674-1056/ac9e95

SPECIAL TOPIC — Quantum frontiers with Rydberg atoms

Floquet quantum state manipulation of a short Rydberg atom array

Jiahui Zhang(张佳慧), Liping Li(李利平)†, Yongjian Wang(王永建), and Bo Wang(王博)

School of Physics and Optoelectronic Engineering, Zhongyuan University of Technology, Zhengzhou 450007, *China*

(Received 7 January 2026; revised manuscript received 26 February 2026; accepted manuscript online 3 March 2026)

We theoretically propose a protocol for coherent quantum state control in a short periodically driven Rydberg atom array. This Floquet engineering effectively suppresses the Rabi coupling and further reshapes Rydberg–Rydberg interactions, enabling precise control of Rydberg dynamics, including population trapping and blockade dynamics. This capability permits the coherent manipulation of targeted quantum states, such as the population-trapping ground state and entangled states with single or double excitations. A key finding is the robustness of these dynamics against variations in the Rydberg atom interaction, allowing for reliable control even in weak interaction regimes. Floquet spectral analysis further reveals that the stability — and eventual breakdown — of the frozen ground state is fundamentally governed by the splitting, convergence, and spacing of quasienergy levels. Moreover, a systematic analysis of parameter dependence identifies precise operational ranges for quantum state control. These results establish a practical framework for Floquet-engineered quantum manipulation, with promising prospects for quantum information processing applications.

Keywords: Rydberg atom array, Floquet engineering, quantum state control, blockade dynamics

PACS: 32.80.Qk, 42.50.Ct

DOI: 10.1088/1674-1056/ae4c70 **CSTR:** 32038.14.CPB.ae4c70

1. Introduction

Rydberg atoms exhibit a range of unique properties including large electric dipole moments,[1–3] strong interactions across a broad electromagnetic spectrum (MHz to THz),[4–7] and energy levels traceable to fundamental constants,[8] which not only underpin their role in cutting-edge quantum technologies like communication,[9–12] computing,[13–16] and gates,[17–22] but also enable their remarkable sensitivity to external driving fields spanning direct current (DC),[1,6,12,14,23] radio frequency (RF),[9,10,12,24] microwave[24–26] and even THz frequencies.[12,14] These features form the cornerstone of advanced electric field sensing and also enable a variety of measurement paradigms. For instance, combining Rydberg atoms with electromagnetically induced transparency (EIT) facilitates highly sensitive, all-optical microwave electrometry, allowing detection of weak fields,[25] precise measurement of strong ones,[26] and all-optical phase retrieval.[24] The use of microwave fields further unlocks sophisticated functionalities, such as continuous-frequency heterodyne detection for communication signals[27] and the engineering of programmable XXZ Hamiltonians in atomic arrays for quantum simulation.[28] Meanwhile, technical innovations like time-dependent pulse optimization methods,[29] multi-channel laser excitation[30] and optimized laser array design[31] continue to push the boundaries of receiver bandwidth and sensitivity. Consequently, the confluence of techniques that include the Stark effect, EIT-AT splitting, and superheterodyne detection establishes Rydberg atoms as a versatile platform for metrology, specialized communications, and imaging.[32–35]

Recently, periodic driving, often referred to as Floquet engineering, has opened up a rich landscape for controlling quantum systems. Through the design of time-periodic Hamiltonians, one can engineer key nonequilibrium states of matter, as exemplified by dissipative dynamics,[36] parity-time symmetry,[37] synthetic gauge fields and topological phases.[38,39] The Floquet approach also extends to quantum resonances,[40] interferometry[41] and frequency modulation effects,[42] depending critically on the interplay between driving and interactions,[43,44] which essentially relates to the fundamental quantum physics concerning coherent manipulation of quantum tunneling,[45,46] population trapping,[47] dynamic localization,[48] coherent destruction of tunneling (CDT),[49] and different types of broadened CDT.[50–54] Thus, periodic driving serves as a powerful tool for quantum simulation, enabling the precise preparation and coherent manipulation of quantum states far from equilibrium.

The synergy between Rydberg atoms and periodic driving allows for advanced quantum state control via correlated Rabi coupling, enabling key implementations like blockade enhancement, antiblockade dynamics, state-dependent population trapping,[55] and dynamical stabilization of both product and entangled states.[47] In recent years, by subjecting neutral atoms to such tailored time-varying fields,[56] there have been many efforts to govern effective Hamiltonians and explore nonequilibrium quantum states beyond the reach of static settings. For instance, a Floquet engineering scheme

†Corresponding author. E-mail: 6716@zut.edu.cn

© 2026 Chinese Physical Society and IOP Publishing Ltd. All rights, including for text and data mining, AI training, and similar technologies, are reserved.

employing a square wave modulated laser field was proposed to manipulate thermalization in a Rydberg atom array.[57] These results are further supported by a range of experimental techniques,[58–61] including modulating the optical field or applying additional radio-frequency fields with Floquet frequency modulation (FFM).[62,63]

In previous works, extensive studies have largely addressed two extremes: Floquet dynamics in periodically driven arrays composed of one or two Rydberg atoms,[47,55] and collective features in large-scale arrays of over a hundred atoms.[15] By contrast, short arrays comprising only a few atoms remain far less explored. Motivated by these considerations, in this work, we investigate coherent quantum state manipulation in a short Rydberg atom array under external periodic driving. Taking a three-atom system as an example, we achieve controlled transitions from an initial state to a target state, while avoiding population of unwanted Rydberg levels. Specifically, transitions between the ground state and single-excitation states are intensively studied by appropriate tuning of the static detuning and periodic driving. We further demonstrate the robustness of the dynamical generation against variations in the van der Waals (vdW) interaction, thereby enabling coherent manipulation even in weak interaction regimes. Remarkably, guided by Floquet quasienergy analysis, we highlight the critical processes of energy-level splitting and convergence that direct the system's evolution. In addition, we also provide a comprehensive discussion of the parameter dependence of population trapping and resonance dynamics, thereby identifying explicit parameter ranges for precise quantum state control.

The structure of this paper is as follows. In Section 2, the model and Hamiltonian of the system are formulated. In Section 3, Floquet manipulation of Rydberg dynamics is presented by precisely tuning the external driving parameters. In Section 4, we discuss two key dynamical behaviors: population trapping and blockade dynamics, as well as the transition between these two regimes. In Section 5, we elucidate the physical mechanism underlying these dynamical behaviors. In Section 6, we systematically investigate the parameter dependence of population trapping and resonance dynamics. The key conclusions of this work are summarized in the last section.

2. Model and Hamiltonian

This work demonstrates coherent quantum state manipulation in a short, one-dimensional Rydberg atom array driven by an external laser field. As a minimal yet nontrivial multibody platform, the three-atom system serves as our model of choice, and the framework developed here can be generalized to larger systems, such as those comprising four or five atoms. A brief analysis of the four-atom array will be presented in Section 6. As schematically shown in Fig. 1(a), we illustrate a driven system of three Rydberg atoms, where the atomic ground state $|g\rangle$ is coherently coupled to the Rydberg state $|e\rangle$. The interactions between Rydberg atoms are characterized by the vdW potential $V_{jk} = C_6/[(j-k)d]^6$, where d is the constant interatomic distance and C_6 is the interaction strength parameter, leading to a nearest-neighbor interaction $V_0 = C_6/d^6$ and a next-nearest-neighbor interaction $V_1 = C_6/(64d^6)$. Within the frozen-gas approximation, the Hamiltonian is governed by[47,55,62]

$$H = \sum_j \left(-\Delta(t)\hat{\sigma}_{ee}^j + \frac{\Omega}{2}\hat{\sigma}_x^j\right) + \sum_{jk} V_{jk}\hat{\sigma}_{ee}^j\hat{\sigma}_{ee}^k, \tag{1}$$

where $\hat{\sigma}_{ab}^j = |a\rangle^j\langle b|$ (where $a,b \in \{g,e\}$, $j = 1,2,3$) represent both projection and transition operations for the jth atom. We define $\hat{\sigma}_x^j = \hat{\sigma}_{ge}^j + \hat{\sigma}_{eg}^j$ and Ω is the Rabi frequency.

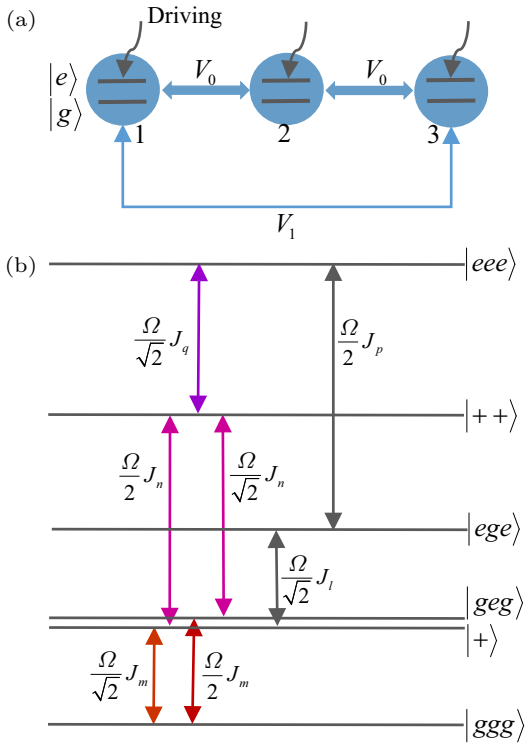


Fig. 1. (a) Schematic of three interacting Rydberg atoms, where each atom features a ground state $|g\rangle$ and a Rydberg state $|e\rangle$, subject to an external periodic driving field. V_0 and V_1 denote the nearest-neighbor and next-nearest-neighbor interactions, respectively. (b) Schematic of effective couplings between six quantum basis states: the ground state $|ggg\rangle$, single-excited states $|+\rangle$ and $|geg\rangle$, double-excited states $|++\rangle$ and $|ege\rangle$, and the triple-excited state $|eee\rangle$. J_m, J_n, J_l, J_p, and J_q are different orders of the Bessel function of the first kind.

In this work, the external driving field applied to the Rydberg states is $\Delta(t) = -\Delta_0 + A\cos(\omega t)$, where Δ_0 is the static DC field, and A and ω are the driving amplitude and frequency of the periodic AC field, respectively. We describe the quantum state in an adiabatic basis using the expansion $|\Psi(t)\rangle = a_{ggg}(t)|ggg\rangle + a_+(t)|+\rangle + a_{geg}(t)|geg\rangle +$

$a_{++}(t)|{+}{+}\rangle + a_{ege}(t)|ege\rangle + a_{eee}(t)|eee\rangle$, where the constituent states include two symmetric entangled states defined by $|+\rangle = (|gge\rangle + |egg\rangle)/\sqrt{2}$ and $|{+}{+}\rangle = (|eeg\rangle + |gee\rangle)/\sqrt{2}$. These six states $\{|ggg\rangle, |+\rangle, |geg\rangle, |{+}{+}\rangle, |ege\rangle, |eee\rangle\}$ form the complete adiabatic basis, with the complex coefficients $\{a_{ggg}(t), a_{+}(t), a_{geg}(t), a_{++}(t), a_{ege}(t), a_{eee}(t)\}$ representing their time-dependent probability amplitudes. In our simulations, all three atoms confined in optical tweezers or a lattice are initialized in their electronic ground state — a well-defined quantum level amenable to precise experimental control. Then the system's dynamics can be explored by numerically solving the Schrödinger equation $\mathrm{i}\hbar\frac{\partial}{\partial t}|\Psi(t)\rangle = H(t)|\Psi(t)\rangle$ (with $\hbar = 1$), from which we compute the time-dependent population probabilities $P_\alpha(t) = |a_\alpha(t)|^2$ ($\alpha \in \{ggg, +, geg, ++, ege, eee\}$) for each adiabatic state, denoted as $\{P_{ggg}, P_+, P_{geg}, P_{++}, P_{ege}, P_{eee}\}$ in the order of the basis states.

Notably, the Hamiltonian in Eq. (1) exhibits explicit time periodicity, $H(t) = H(t+T)$, with driving period $T = 2\pi/\omega$. This periodic structure naturally invites the application of Floquet engineering techniques, which provide a powerful framework for unraveling the dynamical features of our driven three-atom system. Within this approach, the quantum state $|\Psi_\alpha(t)\rangle$ for each adiabatic channel admits an elegant decomposition $|\Psi_\alpha(t)\rangle = \mathrm{e}^{-\mathrm{i}\varepsilon_\alpha t}|\phi_\alpha(t)\rangle$, where ε_α represents the quasienergy and $|\phi_\alpha(t)\rangle$ denotes the Floquet state that inherits the periodicity of the Hamiltonian, $|\phi_\alpha(t)\rangle = |\phi_\alpha(t+T)\rangle$. The quasienergy spectrum emerges from the eigenvalue solution of the time-evolution operator $U(T,0) = \mathcal{T}\exp\left[-\mathrm{i}\int_0^T H(t)\mathrm{d}t\right]$, with $\mathcal{T}$ ensuring proper time ordering.

In order to gain deeper insight into this typical model consisting of three periodically driven Rydberg atoms, we move into a rotating frame by introducing the transformed state $|\Psi'(t)\rangle = \hat{U}(t)|\Psi(t)\rangle$, where the unitary operator is defined as $\hat{U}(t) = \mathrm{e}^{-\mathrm{i}f(t)(\sigma_{ee}^1+\sigma_{ee}^2+\sigma_{ee}^3)+\mathrm{i}tV_0\sigma_{ee}^1\sigma_{ee}^2+\mathrm{i}tV_0\sigma_{ee}^2\sigma_{ee}^3+\mathrm{i}tV_1\sigma_{ee}^1\sigma_{ee}^3}$ with $f(t) = \frac{A}{\omega}\sin(\omega t) - \Delta_0 t$. In the high-frequency approximation, which is valid for $\omega \geq 10\Omega$, we can further obtain the time-independent results by using the Jacobi–Anger expansion, $\mathrm{e}^{\pm\mathrm{i}(A/\omega)\sin(\omega t)} = \sum_{n=-\infty}^{\infty} J_n(A/\omega)\mathrm{e}^{\pm\mathrm{i}n\omega t}$, where n is an integer and $J_n(A/\omega)$ denotes the nth-order Bessel function of the first kind. We systematically derive the effective rotating-frame coupled equations as follows:

$$
\begin{aligned}
\mathrm{i}\frac{\mathrm{d}b_{ggg}(t)}{\mathrm{d}t} &= \frac{1}{\sqrt{2}}\Omega\sum_m J_m\left(\frac{A}{\omega}\right)\mathrm{e}^{\mathrm{i}(m\omega-\Delta_0)t}b_+(t) \\
&\quad + \frac{1}{2}\Omega\sum_m J_m\left(\frac{A}{\omega}\right)\mathrm{e}^{\mathrm{i}(m\omega-\Delta_0)t}b_{geg}(t), \\
i\frac{\mathrm{d}b_+(t)}{\mathrm{d}t} &= \frac{1}{\sqrt{2}}\Omega\sum_m J_m\left(\frac{A}{\omega}\right)\mathrm{e}^{-\mathrm{i}(m\omega-\Delta_0)t}b_{ggg}(t) \\
&\quad + \frac{1}{2}\Omega\sum_n J_n\left(\frac{A}{\omega}\right)\mathrm{e}^{\mathrm{i}(n\omega-\Delta_0-V_0)t}b_{++}(t) \\
&\quad + \frac{1}{\sqrt{2}}\Omega\sum_l J_l\left(\frac{A}{\omega}\right)\mathrm{e}^{\mathrm{i}(l\omega-\Delta_0-V_1)t}b_{ege}(t), \\
i\frac{\mathrm{d}b_{geg}(t)}{\mathrm{d}t} &= \frac{1}{2}\Omega\sum_m J_m\left(\frac{A}{\omega}\right)\mathrm{e}^{-\mathrm{i}(m\omega-\Delta_0)t}b_{ggg}(t) \\
&\quad + \frac{1}{\sqrt{2}}\Omega\sum_n J_n\left(\frac{A}{\omega}\right)\mathrm{e}^{\mathrm{i}(n\omega-\Delta_0-V_0)t}b_{++}(t), \\
\mathrm{i}\frac{\mathrm{d}b_{++}(t)}{\mathrm{d}t} &= \frac{1}{2}\Omega\sum_n J_n\left(\frac{A}{\omega}\right)\mathrm{e}^{-\mathrm{i}(n\omega-\Delta_0-V_0)t}b_+(t) \\
&\quad + \frac{1}{\sqrt{2}}\Omega\sum_n J_n\left(\frac{A}{\omega}\right)\mathrm{e}^{-\mathrm{i}(n\omega-\Delta_0-V_0)t}b_{geg}(t) \\
&\quad + \frac{1}{\sqrt{2}}\Omega\sum_q J_q\left(\frac{A}{\omega}\right)\mathrm{e}^{\mathrm{i}(q\omega-\Delta_0-V_1-V_0)t}b_{eee}(t), \\
\mathrm{i}\frac{\mathrm{d}b_{ege}(t)}{\mathrm{d}t} &= \frac{1}{\sqrt{2}}\Omega\sum_l J_l\left(\frac{A}{\omega}\right)\mathrm{e}^{-\mathrm{i}(l\omega-\Delta_0-V_1)t}b_+(t) \\
&\quad + \frac{1}{2}\Omega\sum_p J_p\left(\frac{A}{\omega}\right)\mathrm{e}^{\mathrm{i}(p\omega-\Delta_0-2V_0)t}b_{eee}(t), \\
\mathrm{i}\frac{\mathrm{d}b_{eee}(t)}{\mathrm{d}t} &= \frac{1}{\sqrt{2}}\Omega\sum_q J_q\left(\frac{A}{\omega}\right)\mathrm{e}^{-\mathrm{i}(q\omega-\Delta_0-V_0-V_1)t}b_{++}(t) \\
&\quad + \frac{1}{2}\Omega\sum_p J_p\left(\frac{A}{\omega}\right)\mathrm{e}^{-\mathrm{i}(p\omega-\Delta_0-2V_0)t}b_{ege}(t), \quad (2)
\end{aligned}
$$

where m, n, q, p, and l are integers, and the column vector $(b_{ggg}(t), \ldots, b_{eee}(t))^{\mathrm{T}}$ describes the transformed quantum state in the rotating frame, where the components correspond to the six adiabatic states. The time-dependent population probabilities $\{P_{ggg}, \ldots, P_{eee}\}$ are obtained directly from these probability amplitudes through $P_\alpha(t) = |b_\alpha(t)|^2$, which track the evolution of the system across the six adiabatic states. From Eq. (2), it is clearly seen that the driving field has significantly renormalized the Rabi couplings, profoundly reshaping the effective couplings between different quantum basis states. In the high-frequency approximation, as shown in Fig. 1(b), if we neglect all the higher-order terms except the resonance ones, the coupling intensities between the ground state and the single-excitation states $|+\rangle$ and $|geg\rangle$ are modified to $\Omega_{\mathrm{eff}} = \Omega J_m/\sqrt{2}$ and $\Omega'_{\mathrm{eff}} = \Omega J_m/2$, where J_m is the abbreviation of $J_m(A/\omega)$. Henceforth, we adopt this abbreviated notation for all Bessel functions. Thus, the transition from the ground state to the single-excitation states is primarily dictated by the mth-order Bessel function satisfying $m\omega = \Delta_0$. Interestingly, the effective coupling between the single-excitation state and the entangled double-excitation state $|{+}{+}\rangle$ is determined by the nth-order Bessel function, with $n\omega = \Delta_0 + V_0$. However, the state exchange between the entangled state $|+\rangle$ and $|ege\rangle$ is mediated by the Bessel function of order l subject to $l\omega = \Delta_0 + V_1$. Given that V_1 is a small perturbation, the relation $m \approx l < n$ follows directly. Consequently, more driving energy ($n\omega$) is needed to couple the single-excitation state to $|{+}{+}\rangle$ than to $|ege\rangle$ ($l\omega$). Moreover, transitions from the

doubly excited states $|{+}{+}\rangle$ and $|ege\rangle$ to the triplet state $|eee\rangle$ require the qth-order and pth-order resonances, respectively, with $q\omega = \Delta_0 + V_0 + V_1$ and $p\omega = \Delta_0 + 2V_0$. These analyses are crucial as they reveal viable pathways for achieving the desired quantum transitions and provide practical alternatives that remain effective under both weak and strong driving conditions. For instance, as shown in Fig. 1(b), we outline three distinct state-manipulation protocols: (1) Blockade dynamics: by enforcing $J_m \neq 0$ and $J_n = J_l = 0$, all higher-order excitations are suppressed. (2) Doubly excited entanglement state $|{+}{+}\rangle$: the pathway $|ggg\rangle \to |+\rangle \to |{+}{+}\rangle$ is realized under the conditions $J_m \neq 0, J_n \neq 0$ and $J_q = 0$. (3) Full triplet excitation $|eee\rangle$: the sequential excitation $|ggg\rangle \to |+\rangle \to |{+}{+}\rangle \to |eee\rangle$ is achieved when all relevant couplings are present, i.e., $J_m, J_n, J_q \neq 0$. Thus, it is the driving-assisted resonances — tied to five key system parameters $\omega, \Delta_0, V_0, V_1$ and A/ω — that collectively determine the Rydberg dynamics.

3. Floquet manipulation of Rydberg dynamics

We begin by preparing all three atoms in the collective ground state, with the total population probabilities satisfying the normalization condition $\sum_\alpha P_\alpha(t) = 1$. Here, the numerical results are obtained using the Runge–Kutta method with a time step of 10^{-2}, and relative and absolute errors of 10^{-3} and 10^{-6}, respectively. For comparison between the results calculated from $b_\alpha(t)$ and the exact numerical ones obtained directly from $a_\alpha(t)$, we plot the evolution of P_α as a function of Ωt in Figs. 2(a)–2(f), with circles and lines representing results without and within the high-frequency approximation, respectively. Their close agreement validates the consistency of our theoretical approaches and confirms that the high-frequency approximation works well in the case of $\omega = 10\Omega$.

We first probe the novel blockade dynamics and present in Figs. 2(a)–2(c) the time evolution of state probabilities P_α by systematically increasing V_0 while keeping $A = 0.5$, $\omega = 0.1$ and $\Delta_0 = 5\omega = 0.5$ fixed. At weak interaction $V_0 = 0.3$ (Fig. 2(a)), the single-excitation states $|+\rangle$ and $|geg\rangle$ (red and black lines) are prominently excited, along with the double-excitation state $|ege\rangle$ (green line). In this regime, atomic transitions from the ground state to both single- and double-excitation states are mediated exclusively by the J_5 Bessel coupling. As V_0 increases to 0.4 (Fig. 2(b)), the doubly excited state $|ege\rangle$ persists with a small but non-negligible probability. With a further increase to $V_0 = 0.6$ (Fig. 2(c)), all higher-order excitations are completely suppressed. Hence, as V_0 increases, V_1 rises in tandem, thereby violating the resonance condition $l\omega = \Delta_0 + V_1$ that governs the coupling between $|+\rangle$ and $|ege\rangle$. As expected, a larger V_0 leads to a more pronounced blockade effect and enables direct population transfer from the ground state to the single-excitation states.

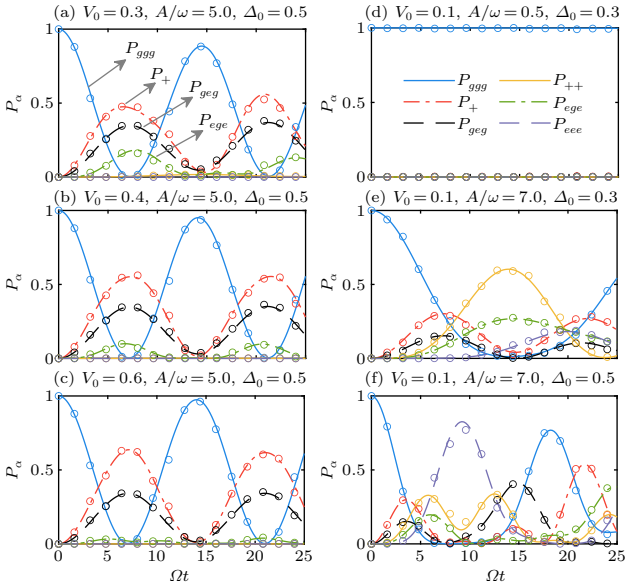


Fig. 2. (a)–(c) P_α versus Ωt for varying interaction V_0 and fixed parameters $A/\omega = 5.0$ and $\Delta_0 = 0.5$ in the cases of (a) $V_0 = 0.3$, (b) $V_0 = 0.4$, and (c) $V_0 = 0.6$. Panels (d)–(f) display three distinct dynamical behaviors with fixed $V_0 = 0.1$: (d) Population trapping at $\Delta_0 = 0.3$, $A/\omega = 0.5$; (e) Generation of the doubly excited entanglement state at $\Delta_0 = 0.3$, $A/\omega = 7.0$; and (f) Excitation of the triplet state at $\Delta_0 = 0.5$, $A/\omega = 7.0$. In all cases, lines and circles represent results with and without the high-frequency approximation, respectively, for $\Omega = 0.01$, $\omega = 0.1$.

To illustrate how the external driving reshapes the tunneling dynamics, we plot P_α versus Ωt in Figs. 2(d)–2(f) to display three distinct dynamical behaviors. For $\Delta_0 = 0.3$, $A/\omega = 0.5$ and $V_0 = 0.1$ (Fig. 2(d)), population trapping at the ground state is observed, which results from the decoupling between the ground state and single-excitation states. This is because both effective couplings $\Omega_{\text{eff}} = \Omega J_3(0.5)/\sqrt{2}$ and $\Omega'_{\text{eff}} = \Omega J_3(0.5)/2$ effectively vanish, preventing transfer out of the ground state. When $A/\omega = 7.0$ while holding $\Delta_0 = 0.3$ and $V_0 = 0.1$ constant (Fig. 2(e)), the double-excitation entanglement state $|{+}{+}\rangle$ reaches a high population probability during the time evolution. Notably, in Fig. 2(f), by adjusting the static detuning $\Delta_0 = 0.5$ while keeping $A/\omega = 7.0$ and $V_0 = 0.1$, the triple-excitation state $|eee\rangle$ also becomes significantly populated. These findings demonstrate that precise quantum state manipulation can be controllably engineered through careful adjustment of the competition between the external driving and vdW interactions. In particular, even with V_0 held fixed at 0.1, the transition between the ground and target states remains fully controllable through adjustment of the DC and periodic driving parameters.

4. Population trapping and blockade dynamics

In this section, we focus on controlling two prominent dynamical effects: population trapping and blockade dynamics, as well as transitions between them. We demonstrate atomic population trapping by calculating the minimum ground-state population probability, $\min P_{ggg}$, within a finite time interval

of 2000 units, as shown in Fig. 3(a), directly highlighting the driving parameter space where the system is trapped in the ground state. For $\Delta_0 = 0.9$, $V_0 = 0.3$, as represented by the solid black line in Fig. 3(a), the three Rydberg atoms remain frozen in the ground state for $A/\omega < 5$. When A/ω increases into the intermediate range $5 < A/\omega < 12$, this frozen state is lifted and $\min P_{ggg}$ drops to zero, signaling the onset of quantum tunneling. Under conditions of strong driving $A/\omega > 12$, $\min P_{ggg}$ returns to unity at specific points such as $A/\omega = 13.35$, indicating a revival of ground-state trapping. Notably, the freezing behavior exhibits little sensitivity to the nearest-neighbor interaction strength V_0, as evidenced by the nearly identical results for $V_0 = 0.5$ and $V_0 = 0.9$, shown as the red and blue lines in Fig. 3(a). The robustness of Rydberg dynamics against V_0 allows for coherent manipulation of Rydberg states even in weak interaction regimes. In essence, this trapping effect arises because the effective couplings between the ground state $|ggg\rangle$ and the single-excited states $|+\rangle$ and $|geg\rangle$, given by $\Omega_{\text{eff}} = \Omega J_9/\sqrt{2}$ and $\Omega'_{\text{eff}} = \Omega J_9/2$, respectively, vanish simultaneously at the chosen parameters corresponding to zeros of the 9th-order Bessel function J_9 (see the gray line in Fig. 3(a)). Consequently, at a series of isolated points $A/\omega = 13.35, 17.24, \ldots$, the atoms are again frozen in their ground states, manifesting as distinct peaks in Fig. 3(a). In addition, while the revival positions are independent of V_0, the interaction strength V_0 modifies the freezing parameter range, and specifically, weaker interactions sustain freezing over a broader range of parameters around the zeros of J_9.

To investigate the effect of static detuning Δ_0 on the ground-state freezing effect, we plot $\min P_{ggg}$ versus A/ω for three different detunings $\Delta_0 = 0.5$, $\Delta_0 = 0.8$, and $\Delta_0 = 1.0$ in Fig. 3(b), with a fixed $V_0 = 0.5$. The value of Δ_0 critically influences the parameter range of A/ω over which population trapping in the ground state persists. For $\Delta_0 = 0.5$, the freezing range is relatively narrow, while for larger detuning magnitudes such as $\Delta_0 = 0.8$ and $\Delta_0 = 1.0$, the parameter range widens accordingly. We also note a series of sharp revival peaks where $\min P_{ggg}$ returns to unity, indicating perfect restoration of ground-state population trapping. These resonant peaks occur at specific driving parameter points corresponding to zeros of Bessel functions, such as $A/\omega = 8.77, 12.34$ for $\Delta_0 = 0.5$ (zeros of J_5), $A/\omega = 12.23$ for $\Delta_0 = 0.8$ (a zero of J_8), and $A/\omega = 14.48$ for $\Delta_0 = 1.0$ (a zero of J_{10}). In each case, the tunneling dynamics are greatly suppressed when the corresponding effective Rabi couplings vanish.

To further characterize the dominant quantum states when the system exits the ground-state freezing regime, we analyze the maximum population probabilities $\max P_\alpha$ versus A/ω during a time interval of 2000 units. At $V_0 = 0.5$ and $\Delta_0 = 0.9$, a comparison between the numerical solutions without and within the high-frequency approximation is presented in Fig. 3(c), where circles and lines correspond to the two models of Eqs. (1) and (2), respectively. As the system exits the freezing regime, it first evolves into a single-excitation state, marked by a significant rise in the maximum population probabilities of $\max P_+$ and $\max P_{geg}$ corresponding to the single-excitation states $|+\rangle$ and $|geg\rangle$. We find that $\max P_+$ (the red line) and $\max P_{geg}$ (the dashed black line) reach approximately 0.66 and 0.33 over the interval $7.5 < A/\omega < 8.0$, and the dynamics are dominated by transitions between the ground state $|ggg\rangle$ and the single-excitation states $|+\rangle$ and $|geg\rangle$, with negligible population in double-excited states such as $|ege\rangle$. This specific population distribution reveals a delocalized single-excitation regime, where the Rydberg single excitation is equally shared among the three atoms. When $A/\omega > 8$, the emergence of $\max P_{ege}$ (the green dot-dashed line) signifies the population of the double-excitation state $|ege\rangle$. As A/ω exceeds 10, a pronounced rise in $\max P_{++}$ (the yellow solid line) occurs, indicating the activation of the entangled double-excitation state $|++\rangle$. This distinct behavior reveals a competition between the two Rydberg double-excitation states, leading to a significant imbalance in their populations when driven. A notable revival of ground-state freezing occurs at $A/\omega = 13.35$, which coincides with a zero of the Bessel function J_9. At this point satisfying $J_9 = 0$, $\max P_{ggg}$ remains at unity, indicating full restoration of the collective ground state. In all cases, the suppression of multi-atom excitations and the revival of ground-state population trapping are consistently governed by the zeros of the corresponding Bessel functions, highlighting a robust mechanism for precise external control of Rydberg dynamics.

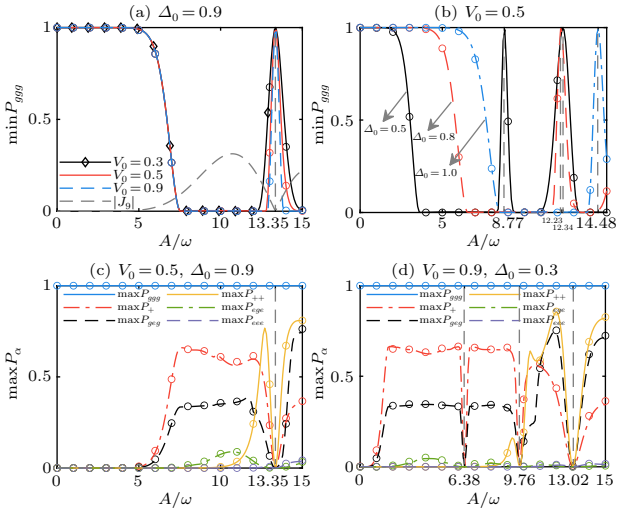


Fig. 3. Minimum population probability $\min P_{ggg}$ as a function of A/ω over $t = 2000$ time units: (a) for $\Delta_0 = 0.9$ with $V_0 = 0.3$ (black line), $V_0 = 0.5$ (red line) and $V_0 = 0.9$ (blue line), compared to the absolute value of the 9th-order Bessel function (gray line); (b) for $V_0 = 0.5$ with detunings $\Delta_0 = 0.5$ (black line), $\Delta_0 = 0.8$ (red line) and $\Delta_0 = 1.0$ (blue line). (c)–(d) Maximum population probability $\max P_\alpha$ versus A/ω over $t = 2000$ time units for: (c) $V_0 = 0.5$, $\Delta_0 = 0.9$; (d) $V_0 = 0.9$, $\Delta_0 = 0.3$. Other parameters: $\omega = 0.1$, $\Omega = 0.01$.

Specifically, our scheme for coherently manipulating the Rydberg dynamics is detailed in Fig. 3(d), through the analysis of $\max P_\alpha$ versus A/ω for parameters $V_0 = 0.9$ and $\Delta_0 = 0.3$. In this regime of strong interaction and weak DC driving, the three-Rydberg-atom system is predominantly excited with a single atom being excited equiprobably, as reflected in the high population probabilities (~ 0.66 and ~ 0.33) of the single-excitation states $|+\rangle$ and $|geg\rangle$, respectively, while the double-excitation state $|ege\rangle$ remains minimally populated–consistent with the difficulty of multi-atom excitation under strong interaction, i.e., the Rydberg blockade effect. As A/ω increases further, the population probabilities of $|+\rangle$ and $|geg\rangle$ deviate from a simple ratio, signaling the breakdown of equiprobable excitation among the three atoms. Concurrently, the doubly excited entangled state $|{+}{+}\rangle$ (yellow curve) gains significant population, implying that strong driving can partially overcome the blockade and promote nearest-neighbor pair excitation. Notably, throughout the entire parameter range, the triple-excitation state $|eee\rangle$ remains unpopulated, demonstrating that the blockade still suppresses simultaneous three-atom excitation, even under stronger driving. Moreover, at the zeros of J_3 (e.g., $A/\omega = 6.38, 9.76, 13.02, \ldots$), the ground state $|ggg\rangle$ becomes fully decoupled from the single-excitation states $|+\rangle$ and $|geg\rangle$. This decoupling suppresses all excitation pathways, resulting in $\max P_{ggg}$ remaining at unity. Our analysis demonstrates that blockade dynamics can be manipulated across a wide parameter range of A/ω, within which the system is restricted to equiprobable single-atom excitation. Moreover, under strong driving, our scheme also offers a pathway to generate a pure entangled double-excitation state $|{+}{+}\rangle$, accomplished by actively suppressing the $|ege\rangle$ state, thereby isolating the desired entangled state. Therefore, studying this nonequilibrium dynamics in a minimal three-atom system represents a critical advance beyond the driven-pair model of Ref. [47], bridging the gap to complex many-body regimes.

5. Physical mechanism behind dynamics

To elucidate the underlying physical mechanism of the dynamics described above, we present the quasienergy spectra in Fig. 4. A closer examination of these spectra reveals how the fundamental parameters A/ω, V_0, and Δ_0 orchestrate the system's behavior through their influence on six quasienergy levels ε_i, where $i = 1, 2, \ldots, 6$. The left column (Figs. 4(a)–4(c)) displays the role of the interaction V_0, whereas the right column (Figs. 4(d)–4(f)) shows the impact of the static detuning Δ_0 on the quasienergy structure. We observe that energy levels ε_3 and ε_6 are most sensitive to variations in the external driving parameter, and ε_4 and ε_5 experience a series of degeneracies as A/ω increases.

For $V_0 = 0.3$ and $\Delta_0 = 0.9$ (Fig. 4(a)), energy levels ε_3 through ε_6 are initially degenerate when $A/\omega < 5$, then split as A/ω increases. In particular, ε_3 and ε_6 display the most pronounced shifts and eventually approach each other at $A/\omega = 13.35$, a value coinciding with a zero of the 9th-order Bessel function. At this same point, ε_4 and ε_5 are degenerate again, as illustrated by the inset in Fig. 4(a). Raising V_0 to 0.5 (Fig. 4(b)), we find that the energy levels still split for $A/\omega > 5$ and converge at the same driving strength $A/\omega = 13.35$. The case of $V_0 = 0.9$ (Fig. 4(c)) provides further confirmation of this trend. However, in the vicinity of $A/\omega = 13.35$, the level spacing between ε_3 and ε_6 progressively narrows as V_0 increases from 0.3 to 0.9. Consequently, the associated population-trapping peak in Fig. 3(a) becomes more confined to a narrower parameter range. We identify that the value of Δ_0 determines where energy levels split and converge, thereby establishing a parameter threshold for transitions between population trapping and tunneling dynamics. Meanwhile, V_0 governs the level spacing around the zeros of J_9, which essentially sets the width of the parameter range over which population trapping occurs.

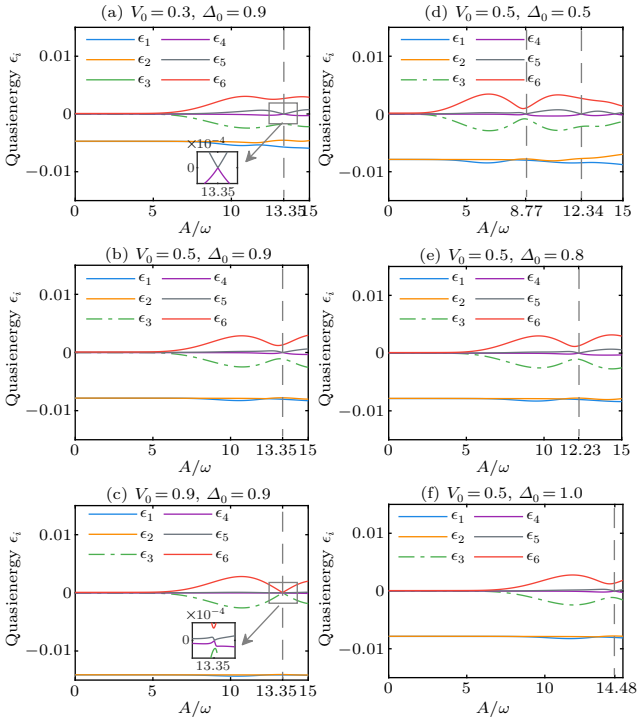


Fig. 4. Quasienergy spectrum as a function of the driving parameter A/ω. (a)–(c) Quasienergy levels for fixed detuning $\Delta_0 = 0.9$ and different interaction strengths: (a) $V_0 = 0.3$, (b) $V_0 = 0.5$ and (c) $V_0 = 0.9$. (d)–(f) Quasienergy levels for fixed $V_0 = 0.5$ with varying detunings: (d) $\Delta_0 = 0.5$, (e) $\Delta_0 = 0.8$ and (f) $\Delta_0 = 1.0$. Other parameters: $\omega = 0.1$, $\Omega = 0.01$.

Furthermore, with the atomic interaction fixed at $V_0 = 0.5$, we examine the Floquet spectra for different static offsets Δ_0 in Figs. 4(d)–4(f). Taking the case $\Delta_0 = 0.5$ (Fig. 4(d)) as an example, levels ε_3–ε_6 begin to split at a smaller A/ω and subsequently converge at two specific points satisfying $A/\omega = 8.77$ and 12.34. These points are attributable to zeros of the 5th-order Bessel function and, notably, precisely

match the two population-trapping peaks, shown by the black solid line in Fig. 3(b). Moreover, the narrower level spacing at $A/\omega = 8.77$ (compared to 12.34) is directly linked to the sharper population-trapping peak observed at that driving parameter in Fig. 3(b). For $\Delta_0 = 0.8$ (Fig. 4(e)), the splitting point shifts to a higher A/ω value compared to Fig. 4(d), implying a broader parameter range for population trapping. The levels then converge at $A/\omega = 12.23$, a zero of the 8th-order Bessel function, which directly accounts for the trapping peak indicated by the red dashed line in Fig. 3(b). A similar correspondence holds for $\Delta_0 = 1.0$ (Fig. 4(f)), where the altered threshold for splitting and convergence aligns with the critical driving parameters given by zeros of the 10th-order Bessel function. Therefore, with increasing A/ω, the system initially remains trapped in the ground state due to quasienergy degeneracy. It then undergoes quantum tunneling following level splitting, and a coherent revival of population trapping emerges due to the driving-induced quasienergy convergence.

6. Parameter dependence

To further investigate the synergistic effect of the external driving field and atomic interactions on the system dynamics, we focus on the evolution of population probability P_{ggg} to identify parameter regimes that are essential for precise quantum state control. To show the effect of the external driving field, we plot P_{ggg} versus A/ω and Ωt in Fig. 5(a) for $V_0 = 0.5$ and $\Delta_0 = 0.5$. The results show that P_{ggg} remains at unity (red region) under weak driving, indicating a population trapping regime independent of evolution time. Beyond a critical A/ω, as indicated by the white auxiliary lines, the three atoms begin to undergo quantum tunneling between the ground state and other excited states. Significantly, population trapping recurs at $A/\omega = 8.77$, corresponding to a zero of the Bessel function J_5, since the effective ground-excited state coupling is again suppressed.

Moreover, to demonstrate the influence of V_0, the evolution of P_{ggg} as a function of both V_0 and Ωt is shown in Fig. 5(b) with fixed parameters $A/\omega = 5.0$ and $\Delta_0 = 0.5$. Interestingly, for small interaction strength ($V_0 < 0.2$), the three atoms initially prepared in the ground state tunnel out without return within the observed evolution time. Increasing V_0 induces coherent tunneling oscillations, allowing P_{ggg} to periodically reach unity at specific times as the three atoms revisit their collective ground state. More importantly, for $V_0 > 0.4$, the dynamical behavior becomes consistent, demonstrating the robustness of the Rydberg dynamics against variations in interaction strength and providing a way to realize stable quantum control in these interaction regimes. Figure 5(c) displays P_{ggg} as a function of Δ_0 and Ωt for $A/\omega = 5.0$ and $V_0 = 0.5$, illustrating the overall effect of Δ_0. It can be seen that the three atoms predominantly remain in the ground state over most of the parameter space (red region), except at a series of resonances $\Delta_0 = m\omega$ (with m an integer). Thus, the mechanism governing the multiple ground-excited state transitions is identified as the mth-order resonance-assisted tunneling.

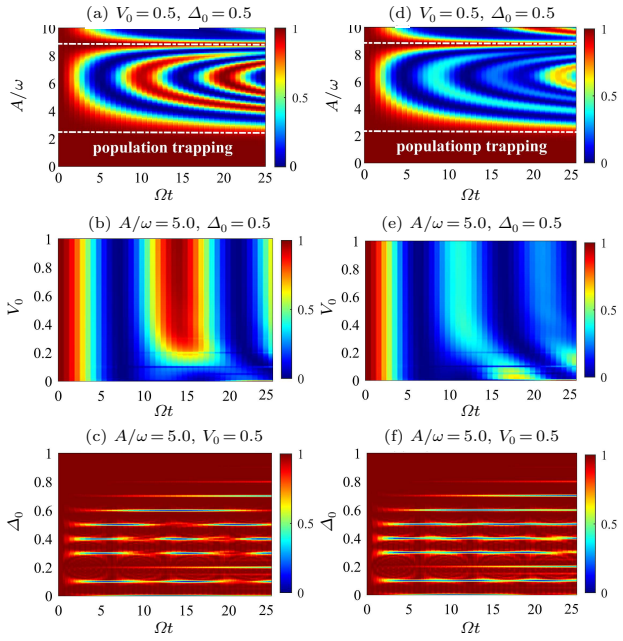


Fig. 5. Comparison of ground-state population dynamics: parameter dependence for three-atom (P_{ggg}, left) and four-atom (P_{gggg}, right) arrays. (a) and (d) P_{ggg} and P_{gggg} versus Ωt as functions of the parameter A/ω, with $V_0 = 0.5$ and $\Delta_0 = 0.5$. (b) and (e) P_{ggg} and P_{gggg} versus Ωt as functions of the parameter V_0, with $A/\omega = 5.0$ and $\Delta_0 = 0.5$. (c) and (f) P_{ggg} and P_{gggg} versus Ωt as functions of the parameter Δ_0, with $A/\omega = 5.0$ and $V_0 = 0.5$. Other parameters are $\omega = 0.1$, $\Omega = 0.01$. The white auxiliary lines in (a) and (d) serve as a reference for the driving parameter range that enables the preparation of population trapping.

To provide a direct comparison, we extend our investigation to a four-atom system. The parameter dependence of P_{gggg} is depicted alongside that of P_{ggg} in Figs. 5(d)–5(f). Using the same parameters as in Fig. 5(a) ($V_0 = 0.5$, $\Delta_0 = 0.5$), Fig. 5(d) plots the time evolution of P_{gggg} versus A/ω, exhibiting an analogous trend. For $A/\omega < 2$, all atoms remain frozen in the ground state, while higher driving A/ω leads to Rydberg state excitation. A key difference from the three-atom system is the absence of a complete population revival to $|gggg\rangle$ within the observed time. Ground-state trapping reoccurs when $A/\omega = 8.77$, corresponding to a zero of J_5.

Figure 5(e) further shows the time evolution of P_{gggg} versus V_0, illustrating robust dynamics for $V_0 > 0.3$. However, unlike the three-atom case, a complete population revival to the ground state does not occur in the four-atom system. Resonant dynamics are shown in Fig. 5(f), which plots the time evolution of P_{gggg} versus Δ_0. Ground-state population trapping is only broken when $\Delta_0 = m\omega$ (with m an integer), thereby enabling quantum state manipulation.

In general, in a short driven Rydberg atom array, the interplay between the external driving and vdW interaction gives rise to rich physical effects. The periodic driving governs the fundamental Rydberg dynamics, while the atomic interaction

serves to suppress higher-order excitations. The DC detuning, in turn, directly determines the emergence of mth-order resonances. These findings establish a versatile pathway for Floquet-based quantum state control in coupled Rydberg atom systems.

7. Conclusion

In summary, we have achieved coherent quantum state manipulation in short driven Rydberg arrays with three and four atoms through the precise control of the interplay among the driving A/ω, the static detuning Δ_0, and the interaction V_0. We identify Δ_0 as the primary parameter governing the stability of ground-state freezing, whereas A/ω dictates the parameter ranges for preparing a target excitation state. The analysis of quasienergy spectra confirms that the breakdown of the frozen state stems from quasienergy level splitting, while the revival of population trapping results from quasienergy convergence. A notable finding is the robust insensitivity of the controlled dynamics to variations in the nearest-neighbor interaction under Floquet modulation, allowing for practical dynamical control even in weak interaction regimes. Furthermore, a comprehensive analysis of how the dynamics depend on key parameters enables the identification of precise parameter regimes necessary for realizing population trapping and driving-induced resonance dynamics. The control scheme developed here for Rydberg state manipulation can be extended to short atom arrays consisting of a small number of Rydberg atoms. These insights not only deepen the understanding of driven Rydberg systems but also open pathways toward practical applications in quantum sensing, communication, and computing.

Acknowledgment

Project supported by the National Natural Science Foundation of China (Grant No. 12005319).

References

[1] Gallagher T F 1988 *Rep. Prog. Phys.* **51** 143
[2] Šibalić N and Adams C S 2018 *Rydberg Physics* (Bristol: IOP Publishing) pp. 8
[3] Li W, Pohl T, Rost J M, Rittenhouse S T, Sadeghpour H R, Nipper J, Butscher B, Balewski J B, Bendkowsky V, Löw R and Pfau T 2011 *Science* **334** 1110
[4] Li W and Lesanovsky I 2012 *Phys. Rev. Lett.* **108** 023003
[5] Li W, Tanner P J and Gallagher T F 2005 *Phys. Rev. Lett.* **94** 173001
[6] Saffman M, Walker T G and Mølmer K 2010 *Rev. Mod. Phys.* **82** 2313
[7] Holloway C L, Gordon J A, Jefferts S, Schwarzkopf A, Anderson D A, Miller S A, Thaicharoen N and Raithel G 2014 *IEEE Trans. Antennas Propag.* **62** 6169
[8] Jentschura U D, Mohr P J and Tan J N 2010 *J. Phys. B: At. Mol. Opt. Phys.* **43** 074002
[9] Song Z, Liu H, Liu X, Zhang W, Zou H, Zhang J and Qu J 2019 *Opt. Express* **27** 8848
[10] Anderson D A, Sapiro R E and Raithel G 2020 *IEEE Aerosp. Electron. Syst. Mag.* **35** 48
[11] Yuan J, Jin T, Xiao L, Jia S and Wang L 2023 *IEEE Antennas Wirel. Propag. Lett.* **22** 2580
[12] Liu B, Zhang L, Liu Z, Deng Z, Ding D, Shi B and Guo G 2023 *Electromagn. Sci.* **1** 0020151
[13] Nielsen M A and Chuang I L 2010 *Quantum Computation and Quantum Information: 10th Anniversary Edition* (Cambridge: Cambridge University Press) pp.13-16
[14] Adams C S, Pritchard J D and Shaffer J P 2020 *J. Phys. B: At. Mol. Opt. Phys.* **53** 012002
[15] Kim K, Kim M, Park J, Byun A and Ahn J 2024 *Sci. Data* **11** 111
[16] Cesa F and Pichler H 2023 *Phys. Rev. Lett.* **131** 170601
[17] Su S L, Sun L N, Liu B J, Yan L L, Yung M H, Li W and Feng M 2023 *Phys. Rev. Appl.* **19** 044007
[18] Su S L, Liang E, Zhang S, Wen J J, Sun L L, Jin Z and Zhu A D 2016 *Phys. Rev. A* **93** 012306
[19] Giudici G, Veroni S, Giudice G, Pichler H and Zeiher J 2025 *PRX Quantum* **6** 030308
[20] Levine H, Keesling A, Semeghini G, Omran A, Wang T T, Ebadi S, Bernien H, Greiner M, Vuletić V, Pichler H and Lukin M D 2019 *Phys. Rev. Lett.* **123** 170503
[21] Xue M, Xu S, Li X and Li X 2024 *Phys. Rev. A* **110** 032619
[22] Chang T H, Wang T N, Jen H H and Chen Y C 2023 *New J. Phys.* **25** 123007
[23] Hogan S D and Merkt F 2008 *Phys. Rev. Lett.* **100** 043001
[24] Schmidt M, Bohaichuk S M, Venu V, Wang R, Kübler H and Shaffer J P 2025 *Phys. Rev. Lett.* **135** 093602
[25] Sedlacek J A, Schwettmann A, Kübler H, Löw R, Pfau T and Shaffer J P 2012 *Nat. Phys.* **8** 819
[26] Anderson D A, Miller S A, Raithel G, Gordon J A, Butler M L and Holloway C L 2016 *Phys. Rev. Appl.* **5** 034003
[27] Liu X H, Liao K Y, Zhang Z X, Tu H T, Bian W, Li Z Q, Zheng S Y, Li H H, Huang W, Yan H and Zhu S L 2022 *Phys. Rev. Appl.* **18** 054003
[28] Scholl P, Williams H J, Bornet G, Wallner F, Barredo D, Henriet L, Signoles A, Hainaut C, Franz T, Geier S, Tebben A, Salzinger A, Zürn G, Lahaye T, Weidemüller M and Browaeys A 2022 *PRX Quantum* **3** 020303
[29] Catalano A G, Dağ C B, Torre G, Giampaolo S M and Franchini F 2025 arXiv:2510.17974 [quant-ph]
[30] Hu J, Jiao Y, He Y, Zhang H, Zhang L, Zhao J and Jia S 2023 *EPJ Quantum Technol.* **10** 51
[31] Wu B, Mao R, Sang D, Sun Z, Liu Y, Lin Y, An Q and Fu Y 2025 *IEEE Trans. Antennas Propag.* **73** 793
[32] Zhang H, Ma Y, Liao K, Yang W, Liu Z, Ding D, Yan H, Li W and Zhang L 2024 *Sci. Bull.* **69** 1515
[33] Minhas T 2024 *Proc. SPIE* **12912** 1291206
[34] Fancher C T, Scherer D R, John M C S and Schmittberger Marlow B L 2021 *IEEE Trans. Quantum Eng.* **2** 3501313
[35] Zhou Z, Yan Z, Liu C, Chen Y and Zhang X F 2025 *Chin. Phys. Lett.* **42** 053705
[36] Zeng Z, Li L, Yang B, Xiao J and Luo X 2020 *Phys. Rev. A* **102** 012221
[37] Yang B, Luo X, Hu Q and Yu X 2016 *Phys. Rev. A* **94** 043828
[38] Eckardt A 2017 *Rev. Mod. Phys.* **89** 011004
[39] Goldman N and Dalibard J 2014 *Phys. Rev. X* **4** 031027
[40] Abanin D A, De Roeck W, Ho W W and Huveneers F 2017 *Phys. Rev. B* **95** 014112
[41] Shevchenko S N, Ashhab S and Nori F 2010 *Phys. Rep.* **492** 1
[42] Silveri M P, Tuorila J A, Thuneberg E V and Paraoanu G S 2017 *Rep. Prog. Phys.* **80** 056002
[43] Ponte P, Chandran A, Papić Z and Abanin D A 2015 *Ann. Phys.* **353** 196
[44] D'Alessio L and Polkovnikov A 2013 *Ann. Phys.* **333** 19
[45] Luo X, Huang J and Lee C 2011 *Phys. Rev. A* **84** 053847
[46] Grifoni M and Hänggi P 1998 *Phys. Rep.* **304** 229
[47] Mallavarapu S K, Niranjan A, Li W, Wüster S and Nath R 2021 *Phys. Rev. A* **103** 023335
[48] Dunlap D H and Kenkre V M 1986 *Phys. Rev. B* **34** 3625
[49] Grossmann F, Dittrich T, Jung P and Hänggi P 1991 *Phys. Rev. Lett.* **67** 516
[50] Li L, Zhao Q, He Q, Zhang J and Wang B 2025 *Phys. Rev. A* **111** 023105
[51] Luo X, Li L, You L and Wu B 2014 *New J. Phys.* **16** 013007
[52] Stockburger J T 1999 *Phys. Rev. E* **59** R4709(R)
[53] Gong J, Morales-Molina L and Hänggi P 2009 *Phys. Rev. Lett.* **103** 133002

[54] Longhi S 2011 *Phys. Rev. A* **83** 034102
[55] Basak S, Chougale Y and Nath R 2018 *Phys. Rev. Lett.* **120** 123204
[56] Dong B Y, Zhou Y, Wang W and Wang T 2025 *Chin. Phys. B* **34** 114203
[57] He Y, Jiao Y, Zhao J and Li W 2026 *Phys. Rev. B* **113** L100303
[58] Omran A, Levine H, Keesling A, Semeghini G, Wang T T, Ebadi S, Bernien H, Zibrov A S, Pichler H, Choi S, Cui J, Rossignolo M, Rembold P, Montangero S, Calarco T, Endres M, Greiner M, Vuletić V and Lukin M D 2019 *Science* **365** 570
[59] Autler S H and Townes C H 1955 *Phys. Rev.* **100** 703
[60] Miller S A, Anderson D A and Raithel G 2016 *New J. Phys.* **18** 053017
[61] Geier S, Thaicharoen N, Hainaut C, Franz T, Salzinger A, Tebben A, Grimshandl D, Zürn G and Weidemüller M 2021 *Science* **374** 1149
[62] Zhao L, Lee M D K, Aliyu M M and Loh H 2023 *Nat. Commun.* **14** 7128
[63] Wu J, Wu J L, Guo F Q, Liu B B, Su S L, Song X K, Ye L and Wang D 2025 *npj Quantum Inf.* **11** 118